



Emergence of elastic chiral Landau levels and snake states

Shuaifeng Li ^{1,2}, Panayotis G. Kevrekidis ³, and Jinkyu Yang⁴

¹*Department of Aeronautics and Astronautics, University of Washington, Seattle, Washington 98105, USA*

²*Department of Physics, University of Michigan, Ann Arbor, Michigan 48109, USA*

³*Department of Mathematics and Statistics, University of Massachusetts, Amherst, Massachusetts 01003, USA*

⁴*Department of Mechanical Engineering, Seoul National University, Seoul 08826, Republic of Korea*



(Received 18 July 2023; revised 13 April 2024; accepted 16 April 2024; published 14 May 2024)

In this paper, we present a method for generating a synthetic gauge field in the vertical direction by linearly modulating the mass term in a Dirac equation model. This allows for the quantization of Landau levels through the generated pseudomagnetic field, with the chiral zeroth Landau level being topologically protected. An elastic snake state is realized using the coupling between the zeroth and the first Landau levels. For demonstration, our theoretical predictions are realized numerically in an elastic medium of truss structures arranged in a honeycomb lattice. Our results, supported by theory and simulations, establish a framework for generating pseudomagnetic fields in elastic systems with potential applications in waveguides and cloaking.

DOI: [10.1103/PhysRevB.109.184109](https://doi.org/10.1103/PhysRevB.109.184109)

I. INTRODUCTION

The physical realization of synthetic gauge fields \mathbf{A} has been an engaging field of condensed matter physics research as it provides an additional degree of freedom for modulating waves [1–7]. Specifically, in phononic systems, the inertness of the elastic waves to the genuine magnetic field makes the realization of pseudomagnetic fields ($\mathbf{B} = \nabla \times \mathbf{A}$) crucial for observing intriguing phenomena such as Landau quantization and artificial Lorentz forces.

In previous studies, the deformation of artificial periodic structures has been used to shift the Dirac cone in the k_x - k_y momentum space, creating the synthetic gauge field in the x - y plane and a corresponding pseudomagnetic field perpendicular to the x - y plane [8–10]. In addition, the variation of geometrical parameters of structures has a similar effect, offering a practical way to realize pseudomagnetic fields [11–13]. This, in turn, facilitates the observation of various magnetic-field-related phenomena in phononic systems such as Landau plateaus and quantum-Hall-like edge states [8, 10–13]. Nevertheless, the exploration of out-of-plane synthetic gauge fields (in-plane pseudomagnetic field) is still limited. Furthermore, an intriguing transport phenomenon, namely the snake state, has been realized in the on-chip structures with opposite pseudomagnetic fields [13]. Such a realization in the uniform pseudomagnetic fields is worth exploring further.

In our paper, we introduce a method to realize the out-of-plane synthetic gauge field (in-plane pseudomagnetic field) by a linear variation of the Dirac effective mass. Thereby, quantized Landau levels can emerge, where the zeroth Landau level is topologically protected. Furthermore, the coupling between the zeroth and first Landau levels can generate the above-mentioned snake states. To realize the theoretical prediction in the real elastic medium, we demonstrate the aforementioned phenomena in a truss model arranged in a honeycomb lattice bearing a gradient in geometrical parameters. In this way, we not only observe the robustness of the zeroth Landau

level, as evidenced by chiral elastic wave propagation against obstacles, but also the elastic snake state, where the wavy propagation trajectory enables the bypassing of obstacles. Our work, supported by the excellent agreement of theoretical prediction and numerical model, provides a promising path towards achieving chiral Landau levels in elastic media, with potential applications in the manipulation of elastic waves.

II. EMERGENCE OF THE CHIRAL LANDAU LEVEL

We start from the periodic honeycomb lattice with two equivalent sites. Therein, the problem of determining the dispersion relation can be cast in the form of a 2×2 eigenvalue problem associated with the following Hamiltonian,

$$H = v(k_x \sigma_x \pm k_y \sigma_y), \quad (1)$$

where v is the Dirac velocity at (k_x, k_y) , and σ_x and σ_y are Pauli matrices. This Hamiltonian maps to the massless Dirac equation associated with locally linear dispersion. When two sites in the unit cell become inequivalent, the broken spatial inversion symmetry essentially introduces a σ_z component into the Hamiltonian which can be expressed as

$$H = v(k_x \sigma_x \pm k_y \sigma_y) + m_K \sigma_z. \quad (2)$$

The effective mass term m_K will break the Dirac degeneracy and open a band gap locally. The width of the band gap is $2|m_K|$ theoretically, which will be elaborated below to show its important role for the formation of the synthetic gauge field.

In Fig. 1(a), we show the schematic of the evolution of band gap when m_K varies from a negative value to positive value. It is obvious that the band gap experiences a open-close-reopen process. Moreover, the sign change of m_K indicates the topological phase transition.

Consider a system where m_K in the Dirac Hamiltonian is varying linearly with respect to x direction ($m_K = qx$). One

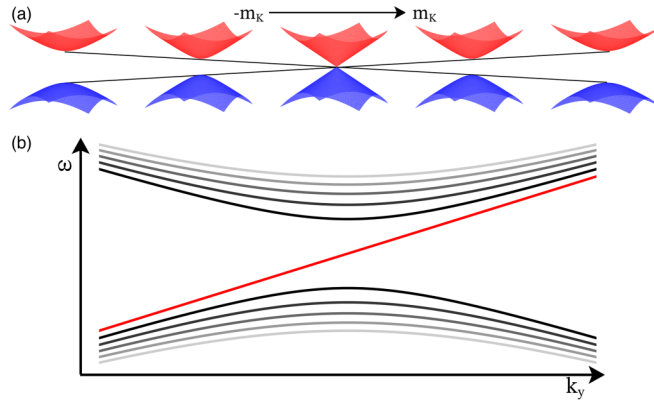


FIG. 1. Emergence of chiral Landau level. (a) The schematic of the evolution of the band gap as a function of effective Dirac mass m_K . (b) The schematic of the dispersion relation with the chiral Landau level in the two-dimensional system using the linear variation of the effective Dirac mass.

can obtain an effective Hamiltonian,

$$H = v(\hat{k}_x\sigma_x \pm \hat{k}_y\sigma_y) + m_K(x)\sigma_z, \quad (3)$$

where \hat{k}_x and \hat{k}_y are the wave-vector operators. Therein, $\hat{k}_x = -i\partial_x$ with the translational symmetry being broken along the x direction, while $\hat{k}_y = k_y$ with the translational symmetry being preserved with the periodic boundary condition along the y direction. According to the form of the Hamiltonian, a vector potential along the z direction $A_z = m_K(x)$ is introduced, suggesting an effective canonical momentum $\hat{k}_z = k_z + A_z$ [$k_z = 0$ in the two-dimensional (2D) system of this study]. Hence, we can expect the in-plane pseudomagnetic field $B_y = \nabla \times A_z$.

With such a pseudomagnetic field affecting our system, the energy levels will be quantized as below (see the theoretical derivation in the Supplemental Material [14]),

$$\omega_n = \begin{cases} \text{sgn}(q)vk_y, & n = 0, \\ \pm\sqrt{v^2k_y^2 + 2n|q|v}, & n \geq 1, \end{cases} \quad (4)$$

where \pm correspond to the \mathbf{K} and \mathbf{K}' valley, respectively. Figure 1(b) shows the schematic of the quantized Landau level. When $n = 0$, corresponding to the zeroth Landau level, the dispersion is linear [red line in Fig. 1(b)], and is determined by the Dirac velocity and the variation of m_K . When $n \geq 1$, corresponding to the higher-order Landau level [grayish line in Fig. 1(b)], the dispersion has the square-root relation, leading to several humps near the zeroth Landau level. Here, we derive the dispersion relation with the chiral Landau levels in a two-dimensional system, whereas previous discussions on such chiral Landau levels are based on three-dimensional Weyl systems [15–17].

III. REALIZATION OF CHIRAL LANDAU LEVEL IN THE ELASTIC MEDIUM

To show the universality of our theory in the elastic system, we realize the aforementioned physical setup using a truss structure with multiple degrees of freedom, which has been widely used in physical and engineering fields. Using the

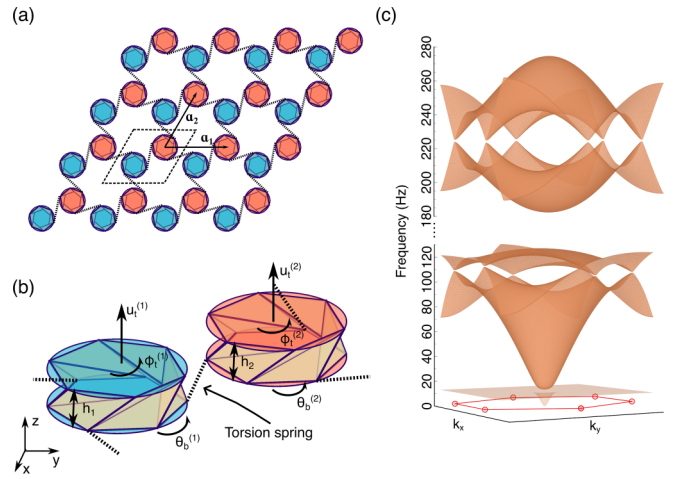


FIG. 2. Design of elastic medium. (a) The top view of the truss structures arranged in the honeycomb lattice. The truss structures are connected by the reverse torsion spring. \mathbf{a}_1 and \mathbf{a}_2 denote two basis vectors of the unit cell enclosed by the black dashed line. (b) The side view of the unit cell composed of two truss structures with heights h_1 and h_2 and rotational angle $\theta_0 = 70^\circ$. Each truss structure has three degrees of freedom u_i , ϕ_i , and θ_b with the bottom disk pinned to the ground. (c) The band structure calculated from the linearized truss model. The Dirac cone emerges in six corners of the Brillouin zone, which is marked as a red line.

discrete truss model, we pursue the effective wave motion in the finite wave number and finite frequency, and analyze truss behaviors near the Dirac cone. As shown by the top view in Fig. 2(a), we design our elastic metamaterials by coupling single truss structures in a honeycomb lattice using reversed torsion springs k_c [18,19]. Note that the truss structure here has two plates on both the top and bottom, six long trusses and six short trusses connecting two plates [Fig. 2(b)], which can broadly represent a Kresling origami, Steward platform, and so on. The design parameters and mechanical parameters, as well as the geometry of the truss structure, are shown in the Supplemental Material [14]. The bottom plates are pinned to the ground, implying that the axial displacement of the bottom plate is zero. The primary unit cell is chosen to be a rhombus enclosed by the black dashed line with basic vectors $\mathbf{a}_1 = (\sqrt{3}a, 0)$ and $\mathbf{a}_2 = (\frac{\sqrt{3}}{2}a, \frac{3}{2}a)$, where $a = 100$ mm is the side length of the honeycomb. The heights are denoted as h_1 and h_2 , while rotation angles are kept the same as $\theta_0 = 70^\circ$. Here, the rotation angle θ_0 indicates the initial angle difference between the bottom plate and top plate after fabrication. Each truss structure has three degrees of freedom: axial displacement of the top plate u_i , and rotational displacements of the top plate ϕ_i and bottom plate θ_b .

When the heights of the two truss structures are the same ($h_1 = h_2 = 20$ mm), the spatial inversion symmetry is preserved. As shown in Fig. 2(c), the associated band structure featuring six bands is calculated using the linearized truss model (see Supplemental Material) [14,20,21], which is the physical realization of the massless Dirac equation. The third and the fourth bands, and the fifth and sixth bands degenerate to form the Dirac cones at a lower frequency and higher frequency.

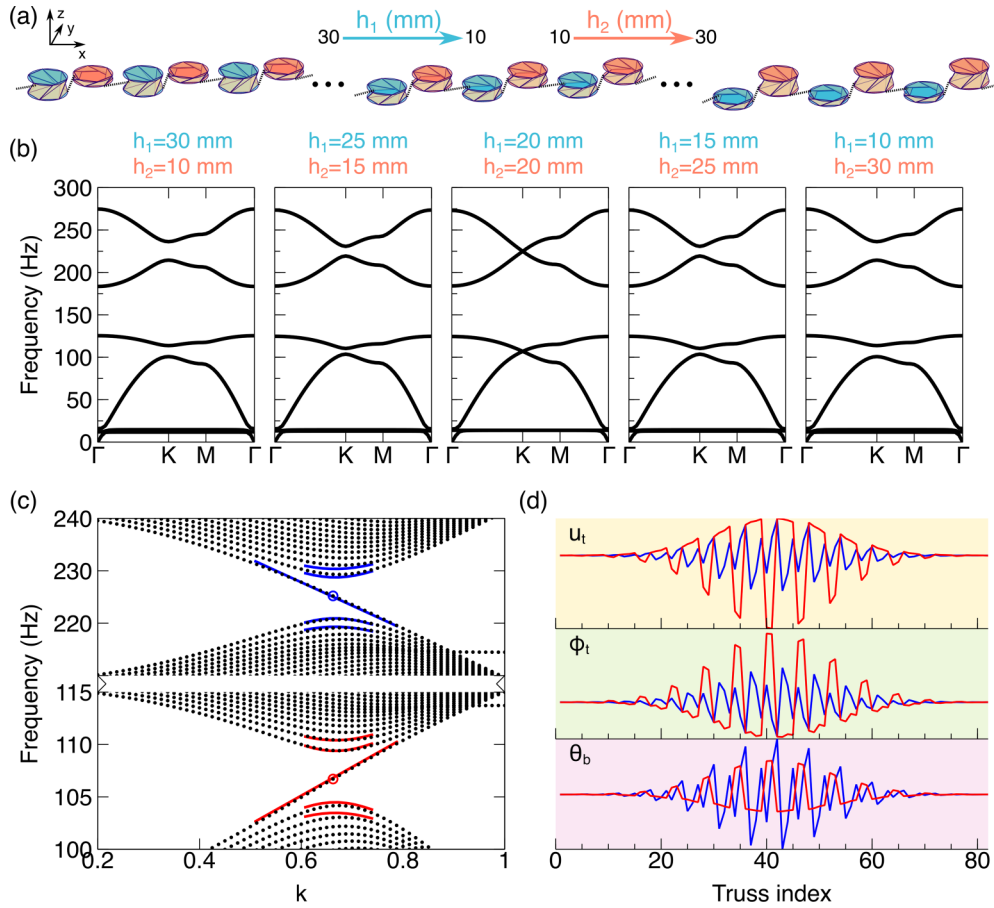


FIG. 3. Synthetic gauge field and Landau level. (a) The schematic of the supercell composed of 41 unit cells (82 truss structures) with a height gradient. The initial heights h_1, h_2 are linearly varying from 30 to 10 mm and from 10 to 30 mm, respectively. (b) The band structure along Γ -K-M- Γ calculated by the unit cell with different configurations. (c) The projected band structure of the supercell under the periodic boundary condition along the y direction. Two ends of the supercell are connected to the wall. The dotted lines denote the calculated Landau levels, while the solid lines denote the theoretical Landau levels. (d) The eigenmodes representing $u_t, \phi_t,$ and θ_b are from the top to the bottom panel. Red and blue lines correspond to the red and blue circles in (c).

When the heights of two trusses are not the same, the spatial inversion symmetry is broken since the coupling behaviors are height dependent (see Supplemental Material [14]). We study the evolution of the band structure when the height difference of two trusses $\Delta h = h_1 - h_2$ varies from 20 to -20 mm, while keeping $h_1 + h_2 = 40$ mm. This variation and such configuration in the form of the supercell with 41 unit cells is shown in Fig. 3(a). The band structures along Γ -K-M- Γ for the corresponding configurations are displayed from left to right in Fig. 3(b). The band gaps between the third and the fourth bands, and the fifth and sixth bands experience the open-close-reopen process, resulting from the mass term in the Dirac equation as explained in Eq. (2) and Fig. 1(a). In addition, m_K can be theoretically calculated by the $\mathbf{k} \cdot \mathbf{p}$ perturbation method [22–26] and is featured by the linear variations along the x direction. Such linear variations are due to the variations of the linear coefficients of truss structures induced by the initial height (see Supplemental Material [14]).

As a result, the magnitude of the generated uniform pseudomagnetic field can be calculated as $B_y = 12.5$ T and $B_y = 19.5$ T for lower frequency and higher frequency, respectively, where the directions of pseudomagnetic field are opposite due to the opposite linear variation of the effective mass term.

Under the pseudomagnetic field, in Fig. 3(c), we show the excellent agreement of the zeroth Landau level and higher-order Landau levels between numerical calculation and theoretical derivation [Eq. (4)] in the vicinity of the \mathbf{K} valley. There appear slight differences when \mathbf{k} is away from the \mathbf{K} valley because the theoretical dispersion relation is approximated based on the approximate continuum Hamiltonian in the \mathbf{K} valley. Furthermore, when n becomes larger (higher-order Landau levels), the difference between the numerical calculation and the theoretical result becomes notable. Note that the boundaries on the two sides connecting to the wall effectively avoid the emergence of the zeroth Landau level from the \mathbf{K}' valley. The eigenmodes of the zeroth Landau level are illustrated in Fig. 3(d), corresponding to red and blue dots at lower and higher frequency. The three degrees of freedom of our truss structure $u_t, \phi_t,$ and θ_b are concentrated near the middle of the supercell (21st unit cell).

To realize the chiral elastic wave propagation, we construct our truss structure by extending the supercell along the direction of the wave vector so that the truss structure with 60×41 unit cells can be formed. We set the chiral excitation source on the axial displacement u_t in the middle to excite the modes subjected to the \mathbf{K} valley corresponding to the zeroth

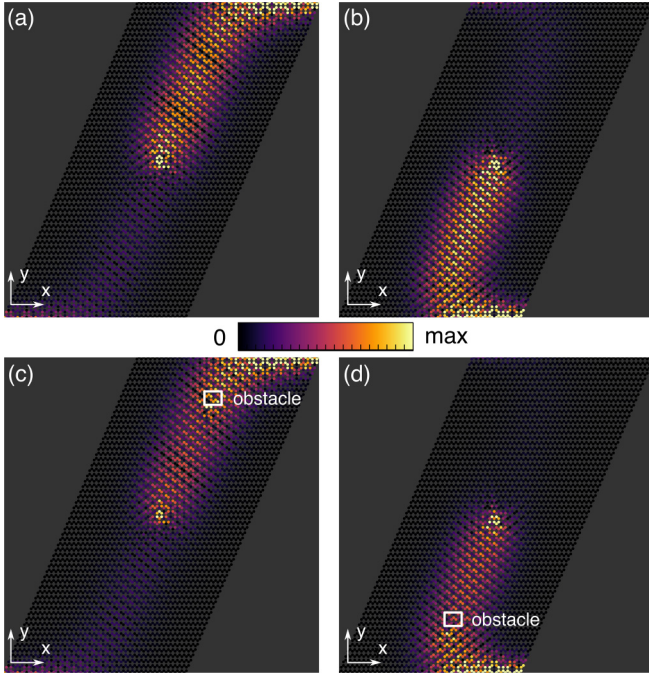


FIG. 4. Robust zeroth Landau level. The field distributions θ_b for the zeroth Landau level in (a) lower frequency and (b) higher frequency. The corresponding cases with obstacles along the propagation path are shown in (c) and (d). Two excitation sources with phase difference are put in the middle. The excitation frequencies are 106 and 225 Hz, respectively.

Landau level. The corresponding frequency response is shown in Fig. 4. Figure 4(a) shows the eigenmode associated with the field distribution of θ_b under the excitation of the lower frequency (106 Hz), where elastic waves can propagate along the $+y$ direction. In stark contrast, elastic waves can also propagate along the opposite direction under the excitation of the higher frequency (225 Hz). This is due to the opposite group velocity of the zeroth Landau level in the two different frequency regions. The time-dependent simulations of elastic wave propagation under corresponding frequencies are shown in the Supplemental Material [14].

Although the Landau levels are considered as bulk states, which are distinct from the topological edge states, the zeroth Landau level is topologically protected [17,27]. This is on account of the negligible intervalley scattering (\mathbf{K} and \mathbf{K}' valleys are widely separated in \mathbf{k} space), resulting in the weak backscattering of elastic waves. To confirm the robustness of the zeroth Landau level, obstacles (truss model with double mass m and rotational inertia j) are put along the wave propagation path while the same excitation is conducted. As shown in Figs. 4(c) and 4(d), the elastic waves feature a linear response along the middle path similar to what is shown in Figs. 4(a) and 4(b), instead of jamming and backscattering. This clearly exhibits the robustness of the transport of the chiral zeroth Landau level. We also notice in Figs. 4(a)–4(d) the elastic wave propagation along the top or bottom edge of the configuration, which may result from the boundary modes due to the free boundary conditions on the two edges subjected to the pseudomagnetic field.

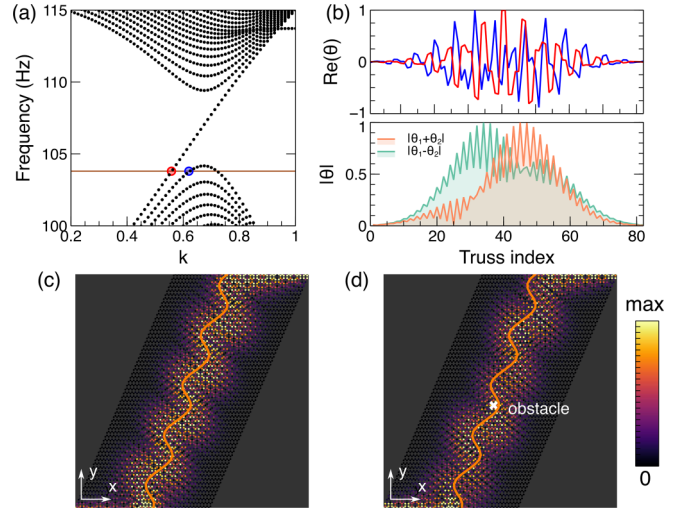


FIG. 5. Elastic snake states. (a) The projected band structure of the supercell at the lower frequency. (b) Top panel: Real parts of the eigenmode θ_{b1} and θ_{b2} along the supercell, corresponding to the red and blue dots in (a). Bottom panel: The defined modes $|\theta_{b1} + \theta_{b2}|$ and $|\theta_{b1} - \theta_{b2}|$. (c) The simulated θ_b distribution under the excitation frequency at 103.9 Hz, corresponding to the solid line in (a). (d) The simulated θ distribution with the obstacle in the middle under the excitation frequency at 103.9 Hz. The theoretical trajectory of the snake state is shown in orange solid line in (c) and (d).

IV. SNAKE STATES

The snake state is a novel transport phenomenon that has been observed in two-dimensional electron gases in p - n junctions of graphene [28–30], when subjected to an external magnetic field. This transport is characterized by a snakelike propagation path, which is driven by the Lorentz force due to the cyclotron motion of electrons in opposite magnetic fields at the interface of two domains with opposite magnetic field [31]. It has been predicted that the pseudomagnetic field can also induce the snake states [13]. In what follows the relation between the zeroth and first Landau levels in the projected band structure shown in Fig. 3(c) is exploited to realize elastic snake states. Note that in stark contrast with the previous work that achieves snake states in opposite pseudomagnetic fields [13], our work realizes snake states in the uniform pseudomagnetic field. It is obvious that the topological phases on two sides are different, essentially providing opposite topological charges, which lays foundations to realize snake states in the uniform pseudomagnetic field.

As mentioned above, the square-root relation of the higher-order Landau level ensures several humps near the zeroth Landau level. We examine the states represented by θ_b of the zeroth and the first Landau levels with the positive group velocity, which are marked by red (θ_{b1} at k_1) and blue dots (θ_{b2} at k_2) in Fig. 5(a). These two states have definite parity with respect to mirror symmetry along the x direction. The real parts of the field distributions in the top panel of Fig. 5(b) reveal that the states θ_{b1} and θ_{b2} have odd and even parities, respectively, suggesting they are orthogonal. In this way, we can define two other orthogonal states: $\langle + | = (\theta_{b1} + \theta_{b2})/\sqrt{2}$ and $\langle - | = (\theta_{b1} - \theta_{b2})/\sqrt{2}$. The states $\langle + |$ and $\langle - |$ tend to be centered

to the right and left of the middle, respectively [bottom panel of Fig. 5(b)]. We can then derive $\theta_{b1} = (|+| + |-|)/\sqrt{2}$ and $\theta_{b2} = (|+| - |-|)/\sqrt{2}$. Using this basis, a general interface state ψ propagating along the middle of the metamaterial can be expressed in the form $\psi = c_1\theta_{b1}e^{ik_1y} + c_2\theta_{b2}e^{ik_2y}$, where c_1 and c_2 are determined by the specific excitation. Assuming that the excitation is placed on the right side of the middle, i.e., $\psi(y=0) = \langle +|$, we have $c_1 = c_2 = 1/\sqrt{2}$. Therefore, $|\langle +|\psi\rangle|^2 = \cos^2(\delta k_y y)$ and $|\langle -|\psi\rangle|^2 = \sin^2(\delta k_y y)$, where $\delta k_y = (k_2 - k_1)/2$. This implies that on the right side ($>20\sqrt{3}a$), the excited state will be oscillating in the form of $\cos^2(\delta k_y y)$. In contrast, on the left side ($<20\sqrt{3}a$), the excited state will be oscillating in the form of $\sin^2(\delta k_y y)$.

Figure 5(a) shows the projected band structure at the lower frequency. Consequently, the excited state will propagate similar to a snake along the middle. The theoretical trajectory of the snake state is shown in orange solid lines in Figs. 5(c) and 5(d), which has a good agreement with the simulation results.

In Fig. 5(c), we illustrate the elastic wave propagation depicting the snake state represented by θ_b . The excitation source on the axial displacement u_t with 103.9 Hz [solid line in Fig. 5(a)] is put at the middle bottom of the truss structure. The clear observation of the elastic snake state is illustrated. The time-dependent simulation of elastic wave propagation is shown in the Supplemental Material [14], where the wavy trajectory is also demonstrated. Since the snake state originates from the bulk and thus does not have robustness, there will be strong backscattering when the elastic waves encounter obstacles. Nevertheless, if the obstacles are placed at the appropriate positions along the path, the wavy snake state can bypass the obstacles, making it appear as if the objects are cloaked [Fig. 5(d)].

V. CONCLUSIONS AND FUTURE CHALLENGES

In conclusion, our paper presents a theoretical realization of an out-of-plane synthetic gauge field and prototypical demonstration using truss structures, leading to the

emergence of the chiral Landau level. The theoretical realization and numerical demonstration are in good agreement, in the appropriate wave-number range, confirming the validity of the long-wavelength approximation used. In the real elastic medium, by leveraging the unique dispersion relation of Landau levels, we have explored the topologically protected chiral elastic wave propagation and the emergence of elastic snake states in one system. Therein, the robust elastic zeroth Landau level can serve as an effective alternative to elastic topological states [32,33]. Although the truss structure in our study is in the centimeter scale, the scalability of this structure and the theoretical prediction allow it to be applied to manipulate elastic waves at different frequencies, potentially contributing to robust waveguiding, vibration control, and object cloaking. Furthermore, though the simulation is based on the truss model, it uses real mechanical properties explored before [21] and can represent many accessible materials and structures such as origami. The future experimental realizations are straightforward but need to overcome the challenges such as damping and fabrication difficulties. Importantly, the features considered herein have been limited to quasicontinuum linear features, in the vicinity of Dirac cones. The configuration, however, proposed herein bears a wide range of interesting phenomena including ones beyond the quasicontinuum approximation, as well as nonlinear features within the band gaps, which is worth exploration in the future study.

ACKNOWLEDGMENTS

J.Y. is grateful for the support by the New Faculty Startup Fund from Seoul National University (SNU). J.Y. also acknowledges the support from SNU-IAMD, SNU-IOER, and National Research Foundation grants funded by the Korea government [Grants No. 2023R1A2C2003705 and No. 2022H1D3A2A03096579 (Brain Pool Plus by the Ministry of Science and ICT)]. This material is based partly upon work supported by the U.S. National Science Foundation under Awards No. PHY-2110030 and No. DMS-2204702 (P.G.K.).

-
- [1] N. R. Cooper, J. Dalibard, and I. B. Spielman, Topological bands for ultracold atoms, *Rev. Mod. Phys.* **91**, 015005 (2019).
 - [2] K. Fang and S. Fan, Controlling the flow of light using the inhomogeneous effective gauge field that emerges from dynamic modulation, *Phys. Rev. Lett.* **111**, 203901 (2013).
 - [3] Q. Lin and S. Fan, Light guiding by effective gauge field for photons, *Phys. Rev. X* **4**, 031031 (2014).
 - [4] Y. Yang, Y. Ge, R. Li, X. Lin, D. Jia, Y.-j. Guan, S.-q. Yuan, H.-x. Sun, Y. Chong, and B. Zhang, Demonstration of negative refraction induced by synthetic gauge fields, *Sci. Adv.* **7**, eabj2062 (2021).
 - [5] L. Lu, J. D. Joannopoulos, and M. Soljačić, Topological photonics, *Nat. Photonics* **8**, 821 (2014).
 - [6] A. B. Khanikaev and G. Shvets, Two-dimensional topological photonics, *Nat. Photonics* **11**, 763 (2017).
 - [7] Z. Yang, F. Gao, X. Shi, X. Lin, Z. Gao, Y. Chong, and B. Zhang, Topological acoustics, *Phys. Rev. Lett.* **114**, 114301 (2015).
 - [8] H. Abbaszadeh, A. Souslov, J. Paulose, H. Schomerus, and V. Vitelli, Sonic Landau levels and synthetic gauge fields in mechanical metamaterials, *Phys. Rev. Lett.* **119**, 195502 (2017).
 - [9] V. Peri, M. Serra-Garcia, R. Ilan, and S. D. Huber, Axial-field-induced chiral channels in an acoustic Weyl system, *Nat. Phys.* **15**, 357 (2019).
 - [10] Z. Yang, F. Gao, Y. Yang, and B. Zhang, Strain-induced gauge field and Landau levels in acoustic structures, *Phys. Rev. Lett.* **118**, 194301 (2017).
 - [11] C. Brendel, V. Peano, O. J. Painter, and F. Marquardt, Pseudomagnetic fields for sound at the nanoscale, *Proc. Natl. Acad. Sci. USA* **114**, E3390 (2017).
 - [12] X. Wen, C. Qiu, Y. Qi, L. Ye, M. Ke, F. Zhang, and Z. Liu, Acoustic Landau quantization and quantum-Hall-like edge states, *Nat. Phys.* **15**, 352 (2019).
 - [13] M. Yan, W. Deng, X. Huang, Y. Wu, Y. Yang, J. Lu, F. Li, and Z. Liu, Pseudomagnetic fields enabled manipulation of on-chip elastic waves, *Phys. Rev. Lett.* **127**, 136401 (2021).

- [14] See Supplemental Material at <http://link.aps.org/supplemental/10.1103/PhysRevB.109.184109> for the simulation setup, perturbation method, theoretical derivation of the Landau level, and time-dependent simulations.
- [15] D. I. Pikulin, A. Chen, and M. Franz, Chiral anomaly from strain-induced gauge fields in Dirac and Weyl semimetals, *Phys. Rev. X* **6**, 041021 (2016).
- [16] A. G. Grushin, J. W. F. Venderbos, A. Vishwanath, and R. Ilan, Inhomogeneous Weyl and Dirac semimetals: Transport in axial magnetic fields and Fermi arc surface states from Pseudo-Landau levels, *Phys. Rev. X* **6**, 041046 (2016).
- [17] H. Jia, R. Zhang, W. Gao, Q. Guo, B. Yang, J. Hu, Y. Bi, Y. Xiang, C. Liu, and S. Zhang, Observation of chiral zero mode in inhomogeneous three-dimensional Weyl metamaterials, *Science* **363**, 148 (2019).
- [18] Y. Wu, R. Chaunsali, H. Yasuda, K. Yu, and J. Yang, Dial-in topological metamaterials based on bistable Stewart platform, *Sci. Rep.* **8**, 112 (2018).
- [19] R. K. Pal, M. Schaeffer, and M. Ruzzene, Helical edge states and topological phase transitions in phononic systems using bilayered lattices, *J. Appl. Phys.* **119**, 084305 (2016).
- [20] S. Li, Y. Miyazawa, K. Yamaguchi, P. G. Kevrekidis, and J. Yang, Geometry-informed dynamic mode decomposition in Kresling origami dynamics, *Extreme Mech. Lett.* **64**, 102082 (2023).
- [21] Y. Miyazawa, C.-W. Chen, R. Chaunsali, T. S. Gormley, G. Yin, G. Theocharis, and J. Yang, Topological state transfer in Kresling origami, *Commun. Mater.* **3**, 62 (2022).
- [22] J. C. Slonczewski and P. R. Weiss, Band structure of graphite, *Phys. Rev.* **109**, 272 (1958).
- [23] Y. Chen, X. Liu, and G. Hu, Topological phase transition in mechanical honeycomb lattice, *J. Mech. Phys. Solids* **122**, 54 (2019).
- [24] S. H. Mousavi, A. B. Khanikaev, and Z. Wang, Topologically protected elastic waves in phononic metamaterials, *Nat. Commun.* **6**, 8682 (2015).
- [25] J. Mei, Y. Wu, C. T. Chan, and Z.-Q. Zhang, First-principles study of Dirac and Dirac-like cones in phononic and photonic crystals, *Phys. Rev. B* **86**, 035141 (2012).
- [26] J. Lu, C. Qiu, S. Xu, Y. Ye, M. Ke, and Z. Liu, Dirac cones in two-dimensional artificial crystals for classical waves, *Phys. Rev. B* **89**, 134302 (2014).
- [27] H. Jia, M. Wang, S. Ma, R.-Y. Zhang, J. Hu, D. Wang, and C. T. Chan, Experimental realization of chiral Landau levels in two-dimensional Dirac cone systems with inhomogeneous effective mass, *Light: Sci. Appl.* **12**, 165 (2023).
- [28] T. Taychatanapat, J. Y. Tan, Y. Yeo, K. Watanabe, T. Taniguchi, and B. Özyilmaz, Conductance oscillations induced by ballistic snake states in a graphene heterojunction, *Nat. Commun.* **6**, 6093 (2015).
- [29] L. Oroszlány, P. Rakyta, A. Kormányos, C. J. Lambert, and J. Cserti, Theory of snake states in graphene, *Phys. Rev. B* **77**, 081403(R) (2008).
- [30] T. K. Ghosh, A. De Martino, W. Häusler, L. Dell'Anna, and R. Egger, Conductance quantization and snake states in graphene magnetic waveguides, *Phys. Rev. B* **77**, 081404(R) (2008).
- [31] J. E. Müller, Effect of a nonuniform magnetic field on a two-dimensional electron gas in the ballistic regime, *Phys. Rev. Lett.* **68**, 385 (1992).
- [32] S. Li, I. Kim, S. Iwamoto, J. Zang, and J. Yang, Valley anisotropy in elastic metamaterials, *Phys. Rev. B* **100**, 195102 (2019).
- [33] S. Li and J. Yang, Topological transition in spiral elastic valley metamaterials, *Phys. Rev. Appl.* **15**, 014058 (2021).